

1 **ARTICLES**

2

3 **Multispectral Photoacoustic Imaging of Tumor Protease**

4 **Activity with a Gold Nanocage-Based Activatable**

5 **Probe**

6

7

8

9 Cheng LIU,¹ Shiyong LI,¹ Yanjuan GU,² Huahua XIONG,³ Wing-tak WONG,² Lei SUN^{1*}

10

11 ¹Department of Biomedical Engineering, The Hong Kong Polytechnic University, Hong Kong
12 SAR, P.R. China,

13 ²Department of Applied Biology and Chemical Technology, The Hong Kong Polytechnic
14 University, Hong Kong SAR, P.R. China,

15 ³Department of Ultrasound, The Second People's Hospital of Shenzhen, Shenzhen, P.R.
16 China.

17

18

19

20

21 **Keywords:** multispectral photoacoustic imaging, activatable photoacoustic probe, tumor
22 protease activity, gold nanocage, molecular photoacoustic imaging

23

24

25

26

27 Please send correspondence to:

28 Lei SUN, Ph.D.

29 Room ST409, Department of Biomedical Engineering,

30 The Hong Kong Polytechnic University,

31 Hong Kong SAR, China, People's Republic of.

32 Phone: (852) 2766 7663

33 Email: lei.sun@polyu.edu.hk

34

35 **ABSTRACT**

36 *Purpose:* Tumor proteases have been recognized as significant regulators in the tumor
37 microenvironment (TME), but the current strategies for *in vivo* protease imaging have tended
38 to focus on the development of probe design rather than the investigation of novel imaging
39 strategy by leveraging the imaging technique and probe. Herein, it is the first report to
40 investigate the ability of multispectral photoacoustic imaging (PAI) to estimate the distribution
41 of protease cleavage sites inside living tumor tissue by using an activatable photoacoustic (PA)
42 probe.

43 *Procedures:* The protease MMP-2 is selected as the target. In this probe, gold nanocages (GNCs)
44 with an absorption peak at ~800 nm and fluorescent dye molecules with an absorption peak at
45 ~680 nm are conjugated *via* a specific enzymatic peptide substrate. Upon enzymatic activation
46 by MMP-2, the peptide substrate is cleaved and the chromophores are released. Due to the
47 different retention speeds of large GNCs and small dye molecules, the probe alters its intrinsic
48 absorption profile and produces a distinct change in the PA signal. A multispectral PAI
49 technique that can distinguish different chromophores based on intrinsic PA spectral signatures
50 is applied to estimate the signal composition changes and indicate the cleavage interaction sites.
51 Finally, the multispectral PAI technique with the activatable probe is tested in solution, cultured
52 cells, and a subcutaneous tumor model *in vivo*.

53 *Results:* Our experiment in solution with enzyme \pm inhibitor, cell culture \pm inhibitor, and *in*
54 *vivo* tumor model with administration of the developed probe \pm inhibitor, demonstrated the
55 probe was cleaved by the targeted enzyme. Particularly, the *in vivo* estimation of the cleavage
56 sites distribution was validated with the result of *ex vivo* immunohistochemistry (IHC) analysis.

57 *Conclusions:* This novel synergy of the multispectral PAI technique and the activatable probe
58 is a potential strategy for the distribution estimation of tumor protease activity *in vivo*.

59 **Introduction**

60 The recent understanding of tumor development has led to a shift from the tumor-centered
61 view to a tumor microenvironment (TME)-centered view [1]. Among the components of the
62 TME, a number of proteases have been implicated as important regulators [2]. Significant
63 progress has been made in the development of different imaging modalities to assess various
64 protease activities *in vivo* [3]. Fluorescence imaging with various fluorescent substrates has
65 become a valued option. When excited, the fluorescent substrates emit light in the red or near-
66 infrared (NIR) ranges, wavelengths with low optical absorbance in biological tissues [4-6].
67 Bioluminescence imaging has also been used to image *in vivo* protease activity using
68 chemiluminescent substrates [7, 8]. Positron emission tomography (PET) and single photon
69 emission computerized tomography (SPECT) have been implemented to detect *in vivo* protease
70 activity by monitoring radiolabeled substrates [9-11]. Similarly, *in vivo* protease activity has
71 been detected by magnetic resonance imaging (MRI) [12-14]. Each of these molecular imaging
72 strategies has intrinsic advantages and disadvantages for protease activity assessment *in vivo*.

73 Photoacoustic imaging (PAI) is an emerging imaging modality that exceeds the optical
74 diffusion limit by detecting acoustic echoes upon light excitation, not only exhibiting a
75 clinically relevant depth of penetration (up to 60 mm) and improved spatial resolution but also
76 providing sensitive optical contrast without ionizing radiation [15, 16]. Although some
77 endogenous molecules, such as hemoglobin and melanin, can generate photoacoustic (PA)
78 contrast, exogenous contrast agents are still needed because most pathophysiological processes
79 elicit little variation in these endogenous PA signals [17]. Fundamentally, conventional
80 exogenous PA contrast agents can produce concentration-dependent contrast only by relying
81 on either passive (e.g., the enhanced permeability and retention effect (EPR)) or active (e.g.,
82 binding to overexpressed cell surface receptors) targeting to sites of interest [18]. Nonetheless,

83 detecting the concentration of a protease does not directly reflect the protease activity in a
84 pathological process because a protease could be expressed as an inactive precursor, which
85 requires activation before the enzymatic function is turned on [19]. Thus, the conventional PA
86 contrast agents generally have difficulties in accurately assessing tumor protease activity. In
87 contrast, activatable imaging probes, which can generate a specific signal by changing their
88 molecular composition only when activated by the targeted molecules, are becoming promising.
89 Considering their advantages, which include enhanced sensitivity and specificity with low
90 background noise and real-time correlation between probes (i.e., activated and non-activated)
91 and disease conditions on a molecular level, the development of activatable PA probes is
92 imperative for the development of *in vivo* protease activity imaging. However, few activatable
93 PA probes for imaging tumor protease activity *in vivo* have been reported except for a small
94 number of recent examples [20-24]. A recent review of the literature on this emerging area
95 summarized versatile design approaches toward activatable PA probes for a variety of
96 molecular targets of interest [25]. Research in this field has tended to focus on the development
97 of novel material and probe design rather than the investigation of novel PA imaging strategy
98 by leveraging the PA technique and activatable PA probe.

99 Nanostructures that exhibit strong optical absorption in the NIR range, including metallic
100 nanoparticles [26], carbon nanotubes [27], graphene-based nanomaterials [28], and organic
101 polymers [29], have been investigated as contrast agents for *in vivo* PAI applications, especially
102 nanostructures based on gold and characterized by different morphologies [17, 30-32]. Gold
103 nanocages (GNCs) are characterized by a single-crystal structure with hollow interiors and
104 ultrathin, porous walls. The localized surface plasmon resonance (LSPR) peaks of GNCs can
105 be easily and precisely tuned to wavelengths in the NIR range by controlling the size and/or
106 wall thickness, making them ideal candidates as contrast agents for PAI in deeper biological
107 tissues. Other significant advantages of GNCs as PAI contrast agents include their large

108 absorption cross sections (almost five orders of magnitude greater than those of conventional
109 organic dyes), low cytotoxicity, and ease of bioconjugation with tumor-specific ligands [33].
110 Previous studies have successfully demonstrated the imaging potential of GNCs as PAI contrast
111 agents for different *in vivo* animal imaging applications [34-36]. Particularly, an enzyme-
112 sensitive probe that was comprised of a gold nanocage and dye molecules linked *via* an enzyme-
113 cleavable peptide was reported [37]. The probe was demonstrated to be a flexible model system
114 for detection of MMP-2 in solution and gel phantom conditions by fluorescence spectroscopy
115 and microscopy tests. And, the potential of the model system as multimodal contrast agent is
116 promising.

117 In this research, the main motivation was to estimate the distribution of protease activity
118 inside living tumor tissue, by utilizing a synergistic method that leverages the advantages of the
119 cutting-edge PAI technique and an activatable PA probe. Thus, we designed an activatable PA
120 probe based on GNCs, as illustrated in **Figure 1**. As an example, we selected the well-studied
121 protease MMP-2 in the family of MMPs, which is overexpressed in various cancer types and
122 associated with key tumorigenesis processes, as the imaging target of interest [38]. The probe
123 produced a strong PA signal contributed by GNCs with an LSPR absorption peak at ~800 nm
124 and by the fluorescent dye Alexa Fluor 680 with an absorption peak at ~680 nm, conjugated by
125 enzymatic peptide substrate. When the peptide was cleaved by the active protease, distinct
126 changes in the optical absorption and PA spectral signature of the as-prepared probe were
127 observed both in solution phase and in a typical live cell culture environment. For *in vivo* study,
128 large GNCs with a size of 30-40 nm were retained inside tumors for an extended period, while
129 the dye molecules were cleared from tumor much more quickly due to their smaller size (~1
130 nm). Therefore, the tumor protease activity could be correlated directly with the PA signal
131 changes [39]. Next, multispectral PAI was used to unmix the PA signal composites from
132 different sources, including exogenous contrast agents and endogenous chromophores (e.g.,

133 deoxygenated/oxygenated hemoglobin and melanin), based on their different intrinsic PA
134 signatures [40-42]. The result showed that the distribution of tumor protease activity *in vivo*
135 could be estimated and visualized by utilizing this novel molecular photoacoustic imaging
136 strategy. To the best of our knowledge, it is the first report of such novel synergy of
137 photoacoustic imaging technique and activatable probe to investigate the *in vivo* distribution
138 estimation of protease activity.

139 **Materials and Methods**

141 **Preparation of the GPD probe**

142 The GNCs were prepared by the reduction of H₂AuCl₄ on a silver nanoparticle framework
143 according to a previously reported method [43]. Briefly, the silver nanoparticles were first
144 synthesized by stirring a silver nitrate solution (0.1 M, 50 ml) with sodium citrate (0.5 M, 1.5
145 ml) and sodium borohydride solutions (0.1 M, 1.5 ml) at room temperature. Larger silver
146 nanoparticles were grown from these stock solutions with additional hydroxylamine
147 hydrochloride. The reducing reaction was initiated by the addition of hydroxylamine
148 hydrochloride solution (0.2 M, 1.5 ml) and stirred for 10 min. Afterwards, silver nitrate solution
149 (0.1 M, 1 ml) was added, and the mixture was stirred overnight. The prepared silver solution
150 (50 ml) was heated to 100°C, and H₂AuCl₄ (25 mM, 800 μl) was added dropwise. The resulting
151 suspension was stirred vigorously for 30 min. All chemicals were obtained from Sigma-Aldrich
152 (Sigma-Aldrich Chemical, St. Louis, MO, USA) unless otherwise stated.

153 The GNCs were functionalized by the addition of the heterobifunctional linker Thiol-PEG-
154 NH₂ (MW ≈ 2,000 g/mol, Laysan Bio, Arab, AL, USA) at 6 mg per 30 ml of GNC solution.
155 The peptide substrate NH₂-GKG***PLGV***RGC-NH₂ (> 95% purity, Bankpeptide Biological
156 Technology, Hefei, China), which possesses a cleavage site between Gly and Val (as indicated
157 by bold italics) [37], was first dissolved in DMSO (10 mg/ml, 200 μl), followed by the addition

158 of N-(3-dimethylaminopro-pylN'-ethylcarbodiimide) hydrochloride (EDC) (2 mg) and N-
159 hydroxysulfosuccinimide (sulfo-NHS) (3 mg) at room temperature with continuous mixing to
160 activate the carboxylic group in the peptide. Then, GNC-PEG-NH₂ was added into the solution
161 to react overnight at room temperature. Excess peptide molecules were removed by
162 ultracentrifugation (Avanti J-25; Beckman Coulter., Fullerton, CA, USA) at 4000 rpm, and the
163 GNC-peptide was purified with Milli-Q water (Millipore, Bedford, MA, USA). Finally, the
164 Alexa Fluor 680 NHS ester (Thermo Fisher Scientific, San Jose, CA, USA) in DMF (1 mg/ml)
165 was coupled to the GNC-peptide through the reactive NHS ester group. After one hour of
166 reaction, the unreacted Dye680 was collected by ultracentrifugation, and the amount of
167 conjugated Dye680 at the surface of the GNCs was determined using a UV-Vis
168 spectrophotometer (Cary 8454; Agilent, Singapore).

169 **Detection of protease activity in solution**

170 Protease MMP-2 catalytic domain (ENZO Life Sciences, Ann Arbor, USA) (0.05 mg/ml,
171 20 μ l) in 2 μ l of TCNB buffer solution (50 mM Tris, 10 mM CaCl₂, 150 mM NaCl, 0.05% Brij
172 35) (pH 7.5) was incubated for 15 min at 37°C before incubation with the GPD probe. The GPD
173 probe (0.45 nM, 200 μ l) was incubated with the prepared MMP-2 catalytic domain (0.05 mg/ml,
174 20 μ l) in the absence or presence of a potent broad spectrum MMP inhibitor GM6001 (Abcam,
175 Cambridge, UK) (10 mM, 2 μ l) that could inhibit the activities of many MMPs including MMP-
176 2, at 37°C for three hrs. The cleaved dye containing the peptide fragment was removed by
177 ultrafiltration. Three trials were conducted in parallel. The UV-Vis absorption spectra of the
178 residual solution were recorded.

179 **Cell culture**

180 The U-87 MG human glioblastoma cell line and MS1 mouse endothelial cell line were
181 purchased from the National Infrastructure of Cell Line Resource (Chinese Academy of Science,

182 Shanghai, China). U-87 MG cells were cultured in
183 Eagle's Minimum Essential Medium (GIBCO, Grand Island, NY, USA) supplemented with
184 10% fetal bovine serum (Invitrogen, Carlsbad, CA, USA) and 1% penicillin-streptomycin
185 (Invitrogen, Carlsbad, CA, USA) at 37°C in a humidified atmosphere of 5% CO₂. MS1 cells
186 were cultured in Dulbecco's Modified Eagle's Medium (DMEM) (GIBCO, Grand Island, NY,
187 USA) supplemented with 5% fetal bovine serum and 1% penicillin-streptomycin at 37°C in a
188 humidified atmosphere of 5% CO₂.

189 **Detection of protease activity in live cells**

190 U-87 MG cells with high MMP-2 expression and MS1 cells with low MMP-2 expression
191 were seeded separately on a 35 mm confocal dish (MatTek, Ashland, USA) at a density of $5 \times$
192 10^4 cells per dish and allowed to grow until 70% confluent. For the inhibitor groups of both cell
193 lines, the medium was removed, and then serum-free medium with 10 μ M MMP-2 inhibitor
194 GM6001 (Abcam, Cambridge, UK) was added to the cell dishes and incubated for 1 hr. Then,
195 the GPD probe was added at a concentration of 0.45 nM and further incubated at 37°C for 3 hr.
196 For the experimental groups of both cell lines, after being washed 3 times with PBS, the cells
197 were incubated with the same concentration of GPD probe in serum-free medium for 3 hrs.
198 Afterwards, the culture medium was removed, and the cells were washed 3 times with PBS.
199 The cells were then counter-stained with Hoechst 33342 (Molecular Probes, Eugene, OR, USA)
200 at a concentration of 0.25 μ g/ml to stain the cell nucleus. Intracellular fluorescence images were
201 captured using a confocal laser scanning microscope (Leica TCS SP8; Leica Microsystems,
202 Wetzlar, Germany) with a 63 \times objective (Ex. 650 nm/Em. 690-740 nm).

203 **PA spectral signature characterization in solution**

204 The PA spectral signatures of nanoparticles were obtained using the Vevo2100 LAZR
205 system (FUJIFILM VisualSonics, Toronto, Canada) with an LZ-250 linear array transducer

206 (center frequency 21 MHz, 256 elements, lateral and axial resolution of 165 and ~ 75 μm ,
207 respectively, maximum imaging depth of 20 mm) to detect transverse coregistered ultrasound
208 and multispectral PA images, and a tunable Nd:YAG laser system (OPOTEK, Carlsbad, CA,
209 680-970 nm, 20 Hz repetition rate, 5 ns pulse width, 50 mJ pulse peak energy) was used to
210 trigger the PA system, exciting the tissue with optical pulses to generate PA signals. Tunable
211 laser light was delivered downward from both long sides of the transducer surface and focused
212 at ~ 10 mm from the transducer surface. The transducer surface was maintained at 10 mm from
213 the Intramedic polyethylene-50 tube (Becton Dickinson, Sparks, MD, USA) containing
214 nanoparticles immersed in DI water, as shown in **Figure S5**.

215 **Xenograft tumor models**

216 All procedures using laboratory animals were approved by the Department of Health, The
217 Government of the Hong Kong Special Administrative Region and the Hong Kong Polytechnic
218 University Animal Subjects Ethics Sub-committee. Tumors were established by the
219 subcutaneous injection of 5×10^6 human glioblastoma U-87 MG cells dissolved in Matrigel
220 (1:1) (BD Biosciences, San Jose, CA, USA) into the right hind limb of 6–8 week-old female
221 nude mice (Centralized Animal Facilities, The Chinese University of Hong Kong, Hong Kong).
222 The mice were used for the experiment when the tumor size reached ~ 100 mm^3 .

223 **The multispectral PAI experiment**

224 The PA images at multiple wavelengths are used to unmix specific chromophore
225 composites, relying on distinct PA spectra signatures. Multispectral PAI can distinguish the
226 cleaved GPD probe from uncleaved GPD probe and relatively unvarying tissue background, by
227 acquiring PA images at multiple wavelengths and estimate the PA chromophore composition
228 contributions based on per-pixel.

229
$$\mu_c^i(\lambda) = \varepsilon_c(\lambda)c_c^i + \varepsilon_u(\lambda)c_u^i + B(\lambda) \quad (1)$$

230 Where $\mu_c^i(\lambda)$ is the wavelength-dependent optical absorption coefficient within pixel i that
231 was acquired by multispectral PAI, $\varepsilon_c(\lambda)$, $\varepsilon_u(\lambda)$, c_c^i , c_u^i are the extinction coefficient of
232 cleaved GPD probe, uncleaved GPD probe and their distribution within the pixel. $B(\lambda)$ is the
233 photoacoustic signal contribution from the background chromophores. The accumulation and
234 distribution of of cleaved GPD probe and uncleaved GPD probe could be estimated by applying
235 linear regression to **Equation (1)** at selected multiple wavelengths. In complicated living tissue
236 background, main background PA signal is contributed by blood (HbO₂ and Hb). In the *in vivo*
237 subcutaneous tumor model, the assumption of the multispectral PAI algorithm is that the optical
238 wavelength-dependence of the laser fluence due to the absorption spectra of tumor tissue
239 background can be neglected.

240 The PA spectral signatures were acquired by a Vevo2100 LAZR System in solution.
241 Images at multiple wavelengths (680 nm, 710 nm, 720 nm, 755 nm, 770 nm, 845 nm, 880 nm,
242 900 nm, 920 nm) were combined with the spectral unmixing software Multiplexer (FUJIFILM
243 VisualSonics, Toronto, Canada) to differentiate specific chromophore composites. Validation
244 testing was conducted by using this strategy to unmix pure chromophores (e.g., fresh chicken
245 blood, GPD probe, GNC, Dye680 and DI water) in PE tubes, as shown in **Figure S5**. *In vivo*
246 multispectral PAI was conducted on a xenograft tumor model using a similar system
247 configuration, as shown in **Figure S8**.

248

249 ***In vivo* photoacoustic (PA) imaging**

250 For intratumoral administration, nude mice bearing U-87 MG tumors were intratumorally
251 injected with GPD probe (0.2 nM, 100 μ l) and imaged at different time points after injection by

252 a Vevo2100 LAZR system at the two representative wavelengths (680 nm and 770 nm). For
253 quantitative calculation, the region of interest (ROI) was drawn over the tumor area, and the
254 average PA signals were measured. The protease activity *in vivo* was quantified using the ratio
255 of PA signal increases at 680 nm and 770 nm:

$$256 \quad \Delta PA_{680} / \Delta PA_{770} = (PA_{680 \text{ postinjection}} - PA_{680 \text{ preinjection}}) / (PA_{770 \text{ postinjection}} - PA_{770 \text{ preinjection}})$$

257 For intravascular administration, nude mice bearing U-87 MG tumors were
258 photoacoustically imaged using a Vevo2100 LAZR system after tail vein injection of the GPD
259 probe (0.9 nM, 200 μ l) at different time points using multispectral PAI.

260 ***Ex vivo* cryosectioning and epi-fluorescence imaging**

261 Immediately after the *in vivo* PAI experiment on the xenograft tumor model, the agar-
262 embedded tumor specimen was stored in freezing medium. The tumor specimens in syringes
263 were snap-frozen at -80°C. After freezing, cryosections through the entire sample were made
264 at 50 μ m intervals along the coronal plane to represent the *in vivo* sectional imaging results.
265 Every 1 mm, the thickness of the section was reduced to 8 μ m to obtain sections suitable for
266 additional histological analysis. Several cryosectioning slices were captured on glass slides.
267 Finally, MMP-2 staining and cell nucleus staining were performed and observed under a Leica
268 DM 2500 upright microscope (Leica Microsystems, Wetzlar, Germany), and pictures taken and
269 automatically digitized using the Panoramic MIDI (3D HISTECH, Budapest, Hungary), and
270 then they were analyzed using the Panoramic Viewer software (3D HISTECH, Budapest,
271 Hungary).

272

273 **Results and Discussion**

274 **Synthesis and characterization of probe**

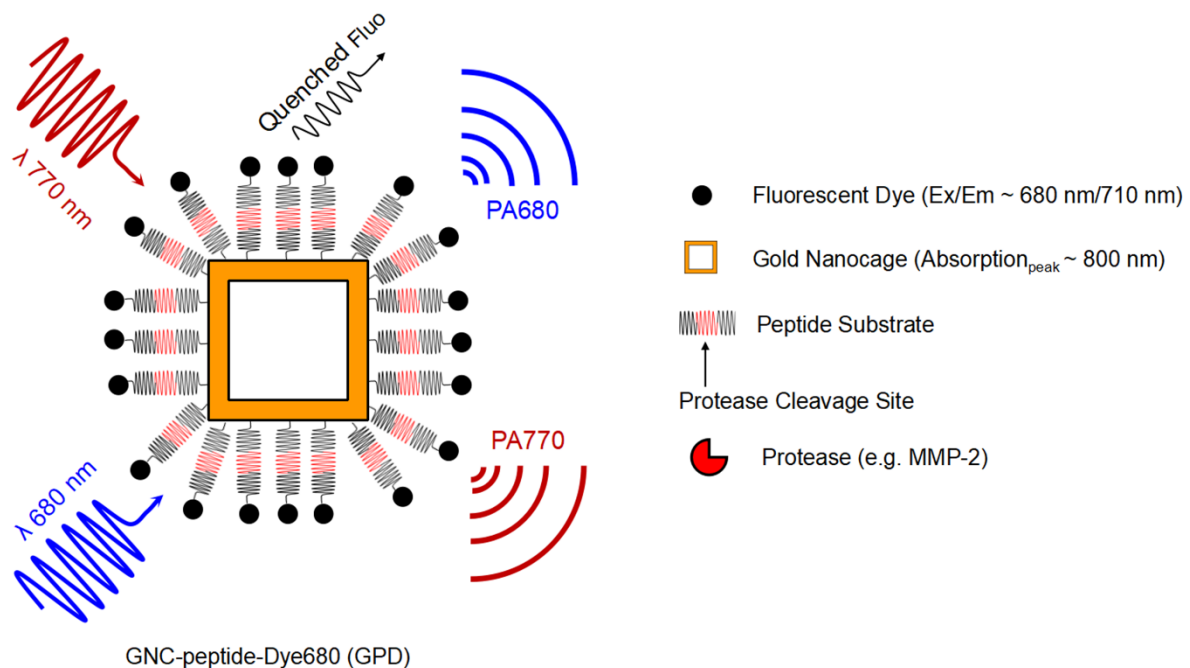
275 **Figure 1** shows the schematic design of the activatable PA probe consisting of two
276 chromophores (i.e., GNCs and fluorescent dye molecules) conjugated *via* an enzymatic peptide
277 substrate specifically cleavable by MMP-2. The resonance absorption peak of GNCs was tuned
278 to 800 nm in the NIR biological window to achieve a greater imaging depth of penetration. The
279 fluorescent dye Alexa Fluor 680 (Dye680) was selected for coupling with the GNCs
280 considering the following properties: 1) its optical absorption peak is distant from that of the
281 GNCs, and 2) it has exceptional resistance to photobleaching. To prepare the probe, GNCs were
282 obtained through a galvanic replacement reaction between silver nanoparticles and a HAuCl₄
283 solution [43]. Next, to improve the stability and biocompatibility of the GNCs and facilitate
284 further conjugation with Dye680, the GNCs were PEGylated *via* conjugation with SH-PEG-
285 NH₂. The Dye680 molecules were then covalently linked to the surface of the PEGylated GNCs
286 by an MMP-2 specific enzymatic peptide substrate. The obtained GNC-peptide-Dye680 (GPD)
287 probe was purified by centrifugation and washed with Milli-Q water.

288 Next, the morphology and size of the GPD probe were characterized by transmission
289 electron microscopy (TEM), as shown in **Figure 2.(A1)**. The TEM image indicated the presence
290 of a 2D lattice fringe, and the spacing was determined to be 2.3 Å, as shown in **Figure 2.(A2)**,
291 which corresponded well to the [111] lattice plane of gold [43]. **Figure 2.(B1)-(B2)** shows the
292 size distribution of the outer and inner diameters of the GPD probe, which have means of 31.7
293 ± 2.6 nm and 20.5 ± 4.8 nm, respectively. The optical absorption spectra of the pure GPD probe,
294 pure GNCs and pure Dye680 were then obtained and are shown in **Figure 2.(C)**. The as-
295 prepared GPD probe showed two characteristic absorption peaks at 680 nm and 800 nm, which
296 corresponded well to those of pure GNCs and Dye680 molecules. The two characteristic
297 absorption peaks also indicated no detectable aggregation in the as-prepared GPD probe. The
298 strong absorption peak of the GPD probe at 680 nm confirmed the successful attachment of
299 Dye680 molecules to GNCs. The payload of Dye680 to GNCs was estimated to be 8 μM of

300 Dye680 per milliliter of GPD probe. Considering the face-centered cubic structure of atoms in
 301 gold nanoparticles and nanocages, the molar concentration of the GPD probe was
 302 approximately 0.905 nM, while the grafting number of Dye680 molecules conjugated on each
 303 particle was approximately 8800. (More details are included in the Supplementary Material.)
 304 The fluorescence emission spectrum of the GPD probe is shown in Figure 2.(D). The peak at
 305 710 nm in the emission spectra of the GPD probe was due to the fluorescence emitted from
 306 Dye680, supporting the successful attachment of Dye680 molecules to GNCs. The fluorescence
 307 emission intensity of the GPD probe was significantly lower than that of pure Dye680 at the
 308 same concentration. This decrease reflected a quenching effect due to nanosurface energy
 309 transfer (NSET) between the conjugated GNCs and Dye680 molecules [37].

310

311



312

313 **Figure 1.** Schematic design of the activatable GPD probe . Before activation, the GPD probe
 314 was expected to produce a strong PA signal with contributions from the GNCs with an LSPR
 315 absorption peak at ~800 nm and from the fluorescent dye Alexa Fluor 680 with an absorption
 316 peak at ~680 nm, conjugated by a specific peptide substrate (cleavable by MMP-2). The as-

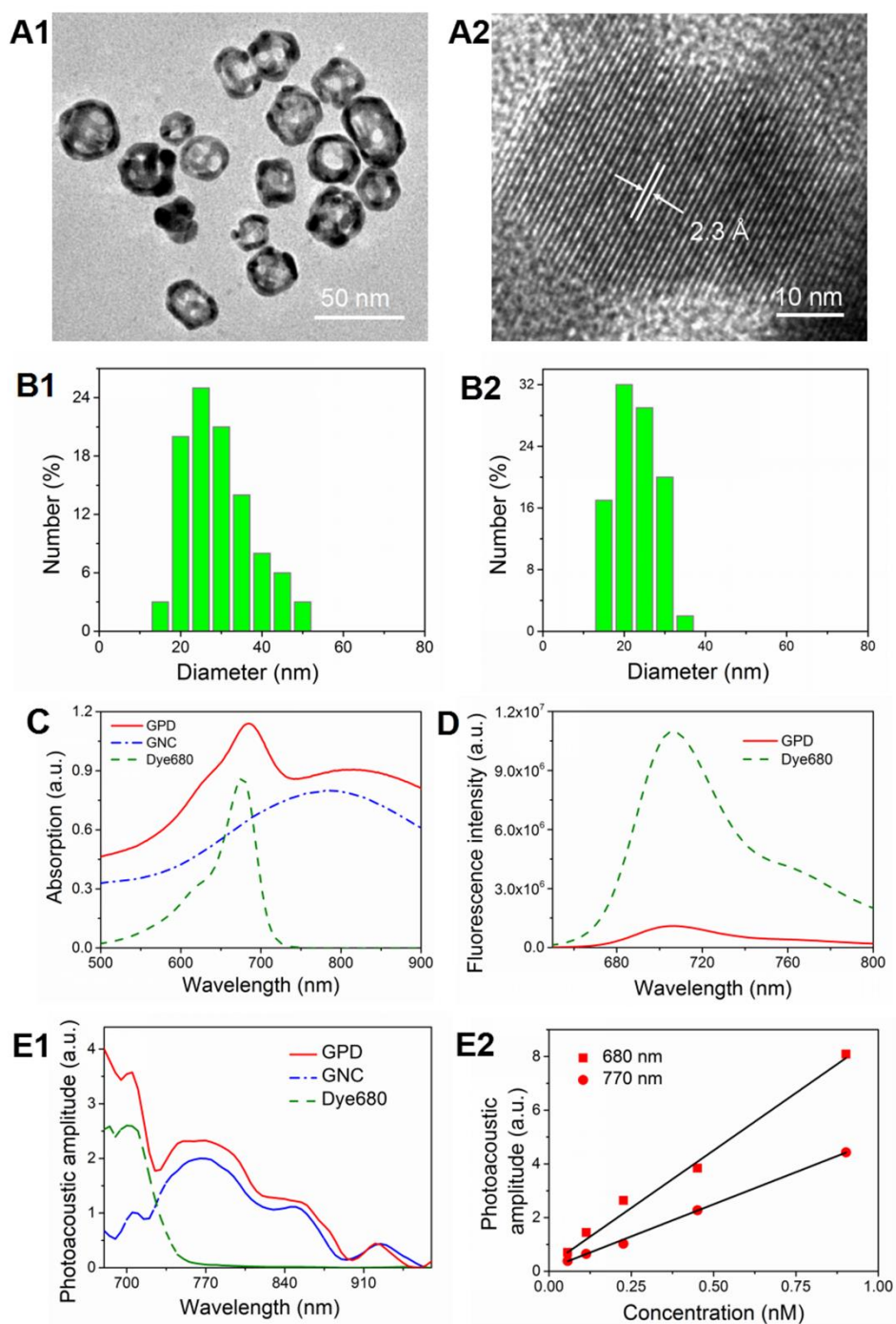
317 prepared GPD probe showed two characteristic PA spectrum peaks at 680 nm and 770 nm,
318 which were close to the optical absorption spectrum peaks. The PA signal changes at 680 nm
319 and 770 nm in multispectral PAI were selected to represent the chromophore composite changes
320 within the GPD probe. In addition, the fluorescence quenching effect between the GNCs and
321 the Dye680 molecules was used to test the synthesis of the GPD probe.

322

323 Furthermore, the PA properties of the as-prepared GNCs were characterized, including the
324 molar extinction cross section coefficient, the molar absorption cross section coefficient and
325 the energy conversion efficiency (ratio of the absorption to the extinction cross section
326 coefficient) [44]. The molar extinction coefficient of the GNCs at the absorption peak
327 wavelength (800 nm) was calculated to be $4.12 \times 10^9 \text{ M}^{-1}\text{cm}^{-1}$, which was much higher than that
328 of hemoglobin ($1 \times 10^3 \text{ M}^{-1}\text{cm}^{-1}$). In addition, the molar absorption coefficient of the GNCs was
329 measured to be $3.89 \times 10^9 \text{ M}^{-1}\text{cm}^{-1}$. (More details are included in the Supplementary Material.)
330 Thus, the energy conversion efficiency was 0.94. This high energy conversion efficiency
331 indicated that the GNCs were much more effective in absorbing than scattering the incident
332 light. Since PAI is an absorption-based imaging modality, the high molar absorption cross
333 section coefficient and high energy conversion efficiency demonstrated that the as-prepared
334 GNCs could be an excellent platform for the development of PA probes. **Figure 2.(E1)** plots
335 the PA intensity as a function of wavelength for the pure GPD probe, pure GNCs and pure
336 Dye680. Each particle has a distinct PA spectral signature. For *in vivo* applications, the PA
337 signals from the GPD probe are usually mixed with signals from other sources (e.g.,
338 hemoglobin) and background noise. Due to the differences in the intrinsic PA spectral
339 signatures, it is feasible to use multispectral PAI to unmix the signals from different composites
340 [16]. The as-prepared GPD probe showed two characteristic PA spectral peaks at 680 nm and
341 770 nm, which were close to the wavelengths of the optical absorption spectral peaks.

342 Consequently, the multispectral PA signal changes at these two wavelengths were selected to
343 represent the composite changes within the GPD probe (i.e., GNCs and dye molecules). In
344 addition, the PA amplitude of the GPD probe at these two representative wavelengths was
345 linearly related to the concentration in the testing range, as shown in **Figure 2.(E2)**.

346
347
348



349
 350 **Figure 2.** Preparation and characterization of the as-prepared GPD probe. (A1) TEM image of
 351 GPD probe (scale bar = 50 nm) and (A2) high-resolution TEM image (scale bar = 10 nm). Size
 352 distribution of the GPD probe: (B1) outer diameter and (B2) inner diameter of GPD probe. (C)
 353 UV-Vis absorption spectra of GPD probe, GNCs and Dye680. (D) Fluorescence emission
 354 spectra of GPD probe and Dye680 (λ_{ex} 710 nm) (at the same concentration as the Dye680

355 molecules attached to the GPD probe). (E1) PA spectral signatures of GPD probe, GNCs and
356 Dye680; (E2) the linear relationship between the PA amplitude and the concentration of the
357 GPD probe at the two representative wavelengths of multispectral PAI.

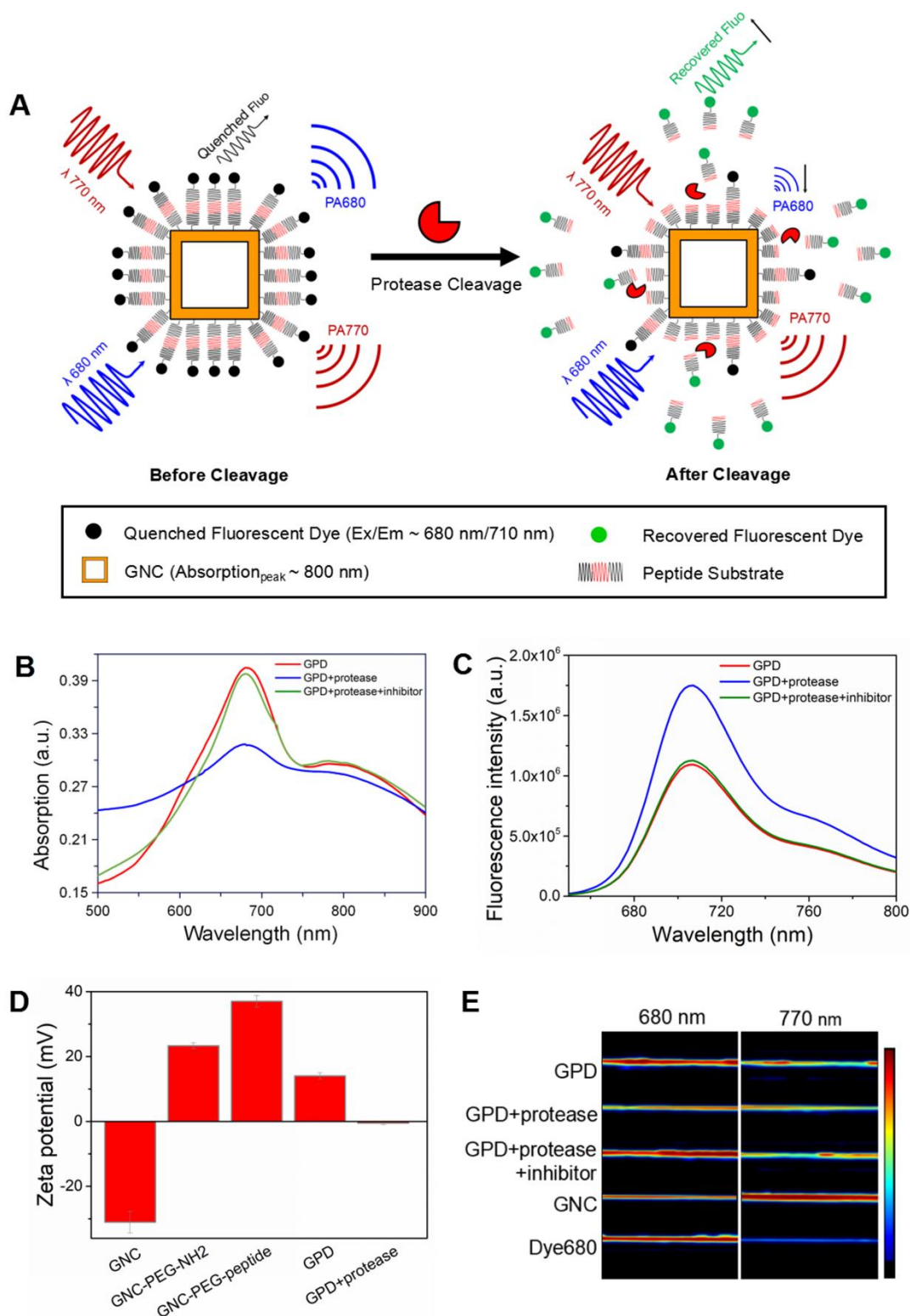
358

359 **Detection of protease activity in solution**

360 The specific enzymatic cleavage of the GPD probe was tested in solution by optical
361 absorption testing, fluorescence emission testing, zeta potential testing and multispectral PAI
362 testing at two representative wavelengths. The experiment was conducted with three parallel
363 groups: 1) GPD probe incubated with protease MMP-2; 2) GPD probe incubated with protease
364 MMP-2 and inhibitor; and 3) pure GPD probe as a control. **Figure 3.(A)** shows the proposed
365 activation mechanism of the GPD probe. **Figure 3.(B)** shows a clear decrease in optical
366 absorption at 680 nm for the GPD probe upon incubation with protease and washing by
367 centrifuge, which suggested that the protease induced peptide cleavage and the release of
368 Dye680 molecules. In contrast, no obvious change was observed in the presence of protease
369 inhibitor, indicating that enzymatic cleavage was inhibited by the inhibitor. The fluorescence
370 emission spectra of the three groups are shown in **Figure 3.(C)**. There was a clear increase in
371 fluorescence from the GPD probe upon incubation with protease due to the recovery of the
372 quenched fluorescence signal from the released Dye680 molecules. In contrast, in the presence
373 of protease inhibitor, no change in fluorescence amplitude could be detected. In addition, the
374 zeta potentials of nanoparticles, including GNCs, PEGylated GNCs (GNC-PEG-NH₂),
375 substrate-conjugated GNCs (GNC-PEG-peptide), GPD probe (GNC-PEG-peptide-Dye680)
376 and GPD probe incubated with protease, were obtained as shown in **Figure 3.(D)**. The zeta
377 potential of PEGylated GNCs (+23.3 mV) was significantly higher than that of GNCs due to
378 the positively charged amine group. After conjugation with the peptide substrate, a higher
379 positive zeta potential (+37.3 mV) was obtained due to the remaining N-terminus from the

380 peptide substrate and the unconjugated amine group from PEG. The zeta potential then
381 decreased to (+14.2 mV) after conjugation with Dye680. Interestingly, a dramatic decrease
382 occurred upon protease incubation. Lastly, nanoparticle-containing tubes were imaged by
383 multispectral PAI at the representative wavelengths, as shown in **Figure 3.(E)**. Compared with
384 the pure GPD probe, there an obvious decrease in the PA signal at 680 nm occurred upon
385 incubation with MMP-2 and washing by centrifuge. In contrast, in the presence of MMP
386 inhibitor, no obvious PA signal change was observed. To summarize, the optical absorption test,
387 fluorescence emission test, zeta potential test and multispectral PAI test all confirmed the
388 specific detection of protease MMP-2 by the GPD probe in solution.

389
390



391
 392 **Figure 3.** Detection of protease activity in solution. (A) Proposed probe activation mechanism.
 393 (B) UV-Vis optical absorption spectra of pure GPD probe, GPD probe incubated with protease
 394 (after washing by centrifuge), and GPD probe incubated with protease MMP-2 and inhibitor

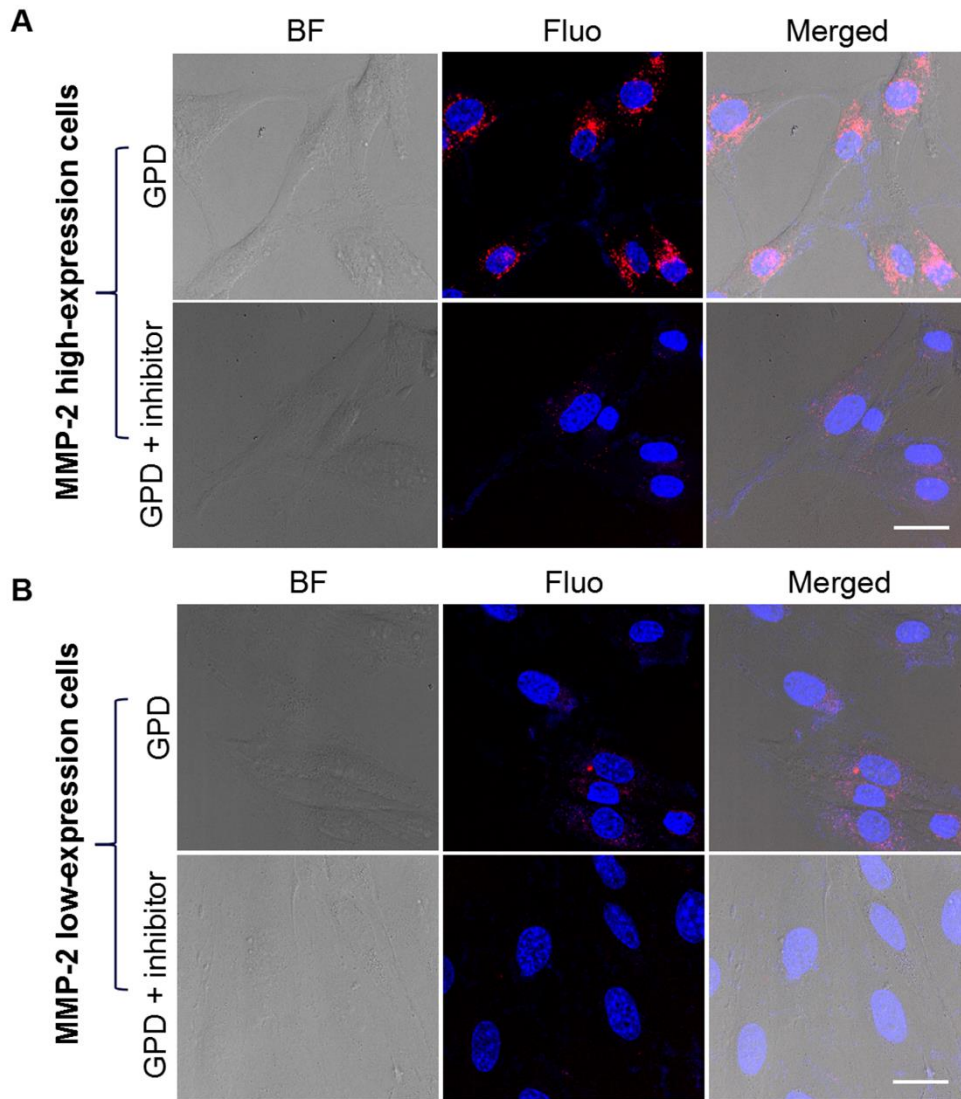
395 (after washing by centrifuge). (C) Fluorescence emission spectra of pure GPD probe, GPD
396 probe incubated with protease (without washing by centrifuge), and GPD probe incubated with
397 protease MMP-2 and inhibitor (without washing by centrifuge). (D) Zeta potential changes for
398 the GNCs, PEGylated GNCs (GNCs-PEG-NH₂), peptide substrate-conjugated GNCs (GNCs-
399 PEG-peptide), GPD probe (GNC-PEG-peptide-Dye680) and GPD probe incubated with
400 protease (after washing by centrifuge). (E) Multispectral PAI at representative wavelengths of
401 pure GPD probe, GPD probe incubated with protease (after washing by centrifuge), GPD probe
402 incubated with protease and inhibitor (after washing by centrifuge), GNC, and Dye680 in tubes.

403

404 **Detection of protease activity in live cells**

405 The enzymatic cleavage of the GPD probe was further tested in typical live cell culture
406 conditions. Two cell lines were selected, U-87 MG for high MMP-2 expression and MS1 for
407 low MMP-2 expression [45]. Both cells were incubated in similar conditions with 0.8 μM
408 Dye680 equivalent of GPD probe for 3 hr in the absence or presence of 10 μM MMP inhibitor.
409 **Figure 4.(A)** shows a significant increase in the intracellular fluorescence signal when U-87
410 MG cells were incubated with the GPD probe and a much lower fluorescence signal in the
411 presence of protease inhibitor. In contrast, no such apparent fluorescence signal difference was
412 observed in MS1 cells, as shown in **Figure 4.(B)**. The results indicated that specific cleavage
413 of the GPD probe was induced by MMP-2 in live cells, as confirmed by the previous results in
414 solution phase.

415



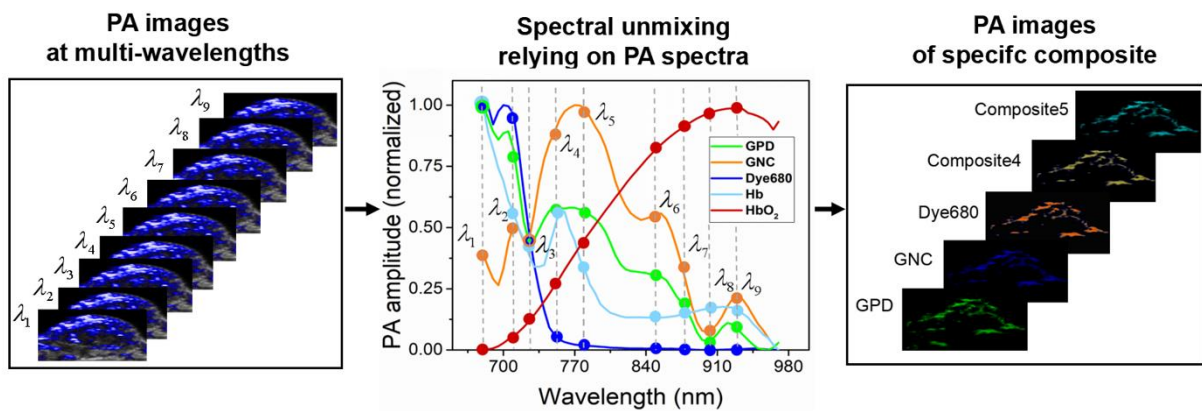
416
 417 **Figure 4.** Detection of protease activity in live cells by confocal fluorescence microscopy. (A)
 418 Cell line with high expression of protease MMP-2 (U-87 MG); and (B) cell line with low
 419 expression of protease MMP-2 (MS1); both types of cells were incubated with GPD probe in
 420 the presence and absence of protease inhibitor. The fluorescence signals were from the
 421 fluorescent dye Alexa Fluor 680. Ex/Em = 683 nm/690-740 nm. Scale bar = 25 μ m. (BF
 422 represents bright field imaging; Fluo represents fluorescence imaging; Merged represents
 423 fluorescence imaging coregistered with bright field imaging.)

424

425

426 **In vivo PAI of protease activity**

427 A human glioblastoma U-87 MG subcutaneous xenograft tumor model was established on
428 nude mice, which has been extensively documented to show high levels of protease MMP-2
429 expression [46]. Images at multiple wavelengths (680 nm, 710 nm, 720 nm, 755 nm, 770 nm,
430 845 nm, 880 nm, 900 nm, 920 nm) were combined with the spectral unmixing software
431 Multiplexer (FUJIFILM VisualSonics, Toronto, Canada) to differentiate specific chromophore
432 composites. The principle of the multispectral PAI technique is shown in **Figure 5**.

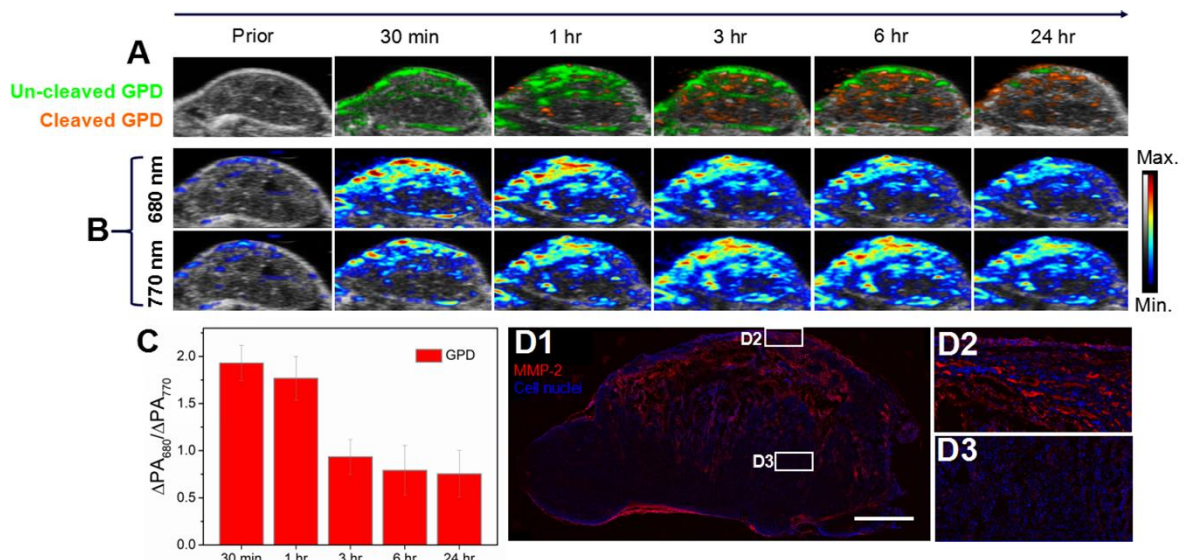


433
434 **Figure 5.** PA images at multiple wavelengths (680 nm, 710 nm, 720 nm, 755 nm, 770 nm, 845
435 nm, 880 nm, 900 nm, 920 nm) are used to unmix specific chromophore composites by relying
436 on distinct PA spectral signatures.

437 A group of animal experiments were conducted *via* tail vein injection of the GPD probe.
438 No obvious multispectral PA signals from the GPD probe were observed in the tumor region
439 immediately after the intravascular injection of the GPD probe. A clear multispectral PA signal
440 (green) from the uncleaved GPD probe appeared ~30 min post injection, as shown in **Figure**
441 **6.(A)**. Afterward, the PA signal from the uncleaved GPD probe exhibited an initial increase and
442 a later decrease, while that from the cleaved GPD probe increased steadily. The early increase
443 in the PA signal from the uncleaved GPD probe suggested its continuous accumulation in the
444 tumor. As higher levels of the GPD probe accumulated and more GPD was cleaved by the
445 protease MMP-2, higher levels of cleaved GPD probe was retained at the cleavage site inside

446 the tumor. On the other hand, because the released Dye680 molecules were cleared away from
 447 the tumor much more quickly, no multispectral PA signal could be detected from Dye680.
 448 Finally, the multispectral PAI at the two representative wavelengths was processed and
 449 quantified and is shown in **Figure 6.(B)** and **Figure 6.(C)**, confirming that the findings
 450 regarding the specific enzymatic cleavage and unique retention process of the GPD probe inside
 451 the tumor were similar to those of the previous intratumoral administration experiment.
 452 Moreover, direct intratumoral administration animal experiments were performed by utilizing
 453 the following four groups of contrast agents: 1) Dye680, 2) GNCs, 3) GPD probe and 4)
 454 protease inhibitor in prior and the GPD probe in order to confirm the specific enzymatic
 455 cleavage of the GPD probe and the different retention times of GNCs and Dye680 molecules
 456 inside tumors *in vivo*. (Details of the intratumoral administration animal experiments are
 457 included in the Supplementary Material **Figure S6.**)

458



459 **Figure 6.** Intravascular administration of the GPD probe monitored by multispectral PAI. (A)
 460 Multispectral PAI of tumor after intravascular injection of GPD probe to estimate the PA signal
 461 composites: un-cleaved GPD probe in green; cleaved GPD probe in gold; ultrasound imaging in
 462 B/W. (B) Multispectral PAI of tumor at two representative wavelengths (680 nm and 770 nm)
 463

464 after intravascular injection of GPD probe. (C) Ratio of PA amplitude increase inside tumor at
465 680 nm and 770 nm after intravascular injection of the GPD probe.
466 $\Delta PA_{680}/\Delta PA_{770} = (PA_{680_{postinjection}} - PA_{680_{preinjection}})/(PA_{770_{postinjection}} - PA_{770_{preinjection}})$. Error bars are based
467 on the standard deviations of 3-4 mice. (D1) *Ex vivo* immunohistochemistry (IHC) analysis
468 (epi-fluorescence imaging) of a cryosection slice from a U-87 MG xenograft tumor specimen,
469 the overall image; (D2) a detailed view of a region with relatively high expression level of
470 MMP-2; (D3) a detailed view of a region with relatively low expression level of MMP-2. MMP-
471 2 staining (red), cell nucleus staining (blue). Scale bar = 2 mm.

472

473 Our *in vivo* results confirmed previous findings reported in the literature that activatable
474 probes have such a “cleavage and retention” mechanism inside tumors, making them a
475 promising approach for the *in vivo* imaging of protease activity in the TME [21, 23]. Upon
476 cleavage, larger nanoparticles would remain in the tumor tissue much longer period than small
477 nanoparticles, which would be quickly cleared after intravascular administration. In addition,
478 our *in vivo* results demonstrated the ability of the synergy of the multispectral PAI and the
479 GNC-based activatable probe to visualize and estimate the distribution of the protease activity
480 *in vivo*. For tail vein injection experiment, the multispectral PAI was useful as a non-invasive
481 visualization tool to estimate the probe accumulation and protease activity cleavage sites inside
482 the tumor. The intratumoral experiment not only confined the probe to the tumor region to
483 eliminate possible non-specific cleavage elsewhere but also prolonged its retention, allowing
484 more interaction time for the enzymatic cleavage of the GPD probe to occur. Furthermore, to
485 validate that the PA contrast change in the tumor region was principally due to existing protease
486 MMP-2, tumor tissues were excised and subjected to immunohistochemistry (IHC) analysis
487 after the *in vivo* experiment. The IHC results revealed elevated MMP-2 expression in some
488 regions inside the tumor, as shown in **Figure 6.(D1)** and **Figure 6.(D2)**, and relatively low

489 expression level of MMP-2, as shown in **Figure 6.(D3)**, which were roughly co-localized with
490 the results visualized and estimated by the multispectral PAI and the GNC-based activatable
491 probe. This molecular PAI strategy exhibited markedly superior imaging contrast owing to its
492 unique PA contrast generation mechanism. More future work is still necessary to explore the
493 precise interpretation of the cleavage process involving the GPD probe and protease *in vivo*.

494

495 **Conclusions**

496 To the best of our knowledge, this paper is the first report of the synergistic strategy of the
497 multispectral PAI technique and the activatable PA probe for *in vivo* distribution estimation of
498 the protease activity in the TME. The as-prepared GPD probe could be cleaved by a specific
499 protease both in solution and in a typical cell culture environment. And, the *in vivo* animal
500 experiment demonstrated the probe was cleaved by the specific enzyme. Particularly, the *in*
501 *vivo* estimation of the cleavage sites distribution was validated with the result of *ex vivo*
502 immunohistochemistry (IHC) analysis. The results could provide valuable information for the
503 development of various *in vivo* protease imaging applications.

504

505

506 **Abbreviations**

507 PAI: photoacoustic imaging; GNC: gold nanocage; TME: tumor microenvironment; NIR:
508 near-infrared; PET: Positron emission tomography; SPECT: single photon emission
509 computerized tomography; MRI: magnetic resonance imaging; PA: photoacoustic; EPR:
510 enhanced permeability and retention effect; LSPR: localized surface plasmon resonance;
511 Dye680: fluorescent dye Alexa Fluor 680; GPD: GNC-peptide-Dye680; TEM: transmission
512 electron microscopy; NSET: nanosurface energy transfer; BF: bright field imaging; Fluo:
513 fluorescence imaging; Merged: fluorescence imaging coregistered with bright field imaging;
514 Hb: de-oxygenated hemoglobin; HbO₂: oxygenated hemoglobin; IHC: immunohistochemistry.

515

516 **Supplementary Material**

517 **Supplementary Results:**

518 **Figure S1.** Dynamic light scattering size distribution of GNCs.

519 **Figure S2.** Dynamic light scattering size distribution of GPD probe.

520 **Figure S3.** Cell cytotoxicity of GPD probe to U-87 MG cells (n = 5, *p < 0.05).

521 **Figure S4.** The linear relationship between the optical absorption amplitude and the
522 concentration of GNCs at the absorption peak wavelength ($\lambda_{ab} = 800$ nm).

523 **Figure S5.** The validation of the multispectral PAI technique in solution.

524 **Figure S6.** Intratumoral administration of the GPD probe by PAI at two representative
525 wavelengths.

526

527 **Supplementary Methods:**

528 **Dynamic light scattering (DLS) profiles of nanoparticles**

529 **Toxicity of the GPD probe**

530 **Molar concentration of nanoparticles**

531 **Determination of the molar extinction/absorption coefficient of the GNCs**

532 **Figure S6.** The experimental setup for multispectral PAI of nanoparticles in PE tubes using a
533 Vevo2100 LAZR System.

534 **The multispectral PAI experiment**

535 **Figure S7.** The experimental setup for multispectral PAI of nanoparticles in PE tubes using a
536 Vevo2100 LAZR System.

537 **Figure S8.** *In vivo* multispectral PAI was conducted on a xenograft tumor model using a
538 Vevo2100 LAZR System.

539

540 **Acknowledgements**

541
542 This work was supported in part by the Hong Kong Innovation and Technology Fund
543 (GHP/009/14SZ), Shenzhen Science, Technology and Innovation Commission research grant
544 (SGLH20150216172854731), Health and Medical Research Fund of Food and Health Bureau
545 of Hong Kong (01121836 and 03144266), National Natural Science Foundations of China
546 (11674271), The Hong Kong Polytechnic University internal grant (4-BCAP and 4-BCDP).
547 The authors acknowledge the use of the University Research Facility in Life Sciences (ULS).
548 There is no conflict of interest to disclose.

549

550 **References**

- 551 1. Hanahan D, Weinberg RA. Hallmarks of cancer: the next generation. *Cell*. 2011; 144:
552 646-74.
- 553 2. Quail DF, Joyce JA. Microenvironmental regulation of tumor progression and
554 metastasis. *Nat Med*. 2013; 19: 1423-37.
- 555 3. Razgulin A, Ma N, Rao J. Strategies for *in vivo* imaging of enzyme activity: an overview
556 and recent advances. *Chem Soc Rev*. 2011; 40: 4186-216.
- 557 4. Ding S, Blue RE, Morgan DR, Lund PK. Comparison of multiple enzyme activatable
558 near infrared fluorescent molecular probes for detection and quantification of inflammation in
559 murine colitis models. *Inflamm Bowel Dis*. 2014; 20: 363.
- 560 5. Yang H-J, Kong Y, Cheng Y, Janagama H, Hassounah H, Xie H, et al. Real-time
561 Imaging of Mycobacterium tuberculosis, Using a Novel Near-Infrared Fluorescent Substrate. *J*
562 *Infect Dis*. 2017; 215: 405-14.
- 563 6. Gu K, Xu Y, Li H, Guo Z, Zhu S, Zhu S, et al. Real-time tracking and *in vivo*
564 visualization of β -galactosidase activity in colorectal tumor with a ratiometric near-infrared
565 fluorescent probe. *J Am Chem Soc*. 2016; 138: 5334-40.
- 566 7. Kim Y-P, Daniel WL, Xia Z, Xie H, Mirkin CA, Rao J. Bioluminescent nanosensors for
567 protease detection based upon gold nanoparticle–luciferase conjugates. *Chem Commun*. 2010;
568 46: 76-8.
- 569 8. Zeng T, Zhang T, Wei W, Li Z, Wu D, Wang L, et al. Compact, programmable, and
570 stable biofunctionalized upconversion nanoparticles prepared through peptide-mediated phase
571 transfer for high-sensitive protease sensing and *in vivo* apoptosis imaging. *ACS Appl Mater*
572 *Interfaces*. 2015; 7: 11849-56.

- 573 9. Chuang C-H, Chuang K-H, Wang H-E, Roffler SR, Shiea J-t, Tzou S-C, et al. *In vivo*
574 positron emission tomography imaging of protease activity by generation of a hydrophobic
575 product from a noninhibitory protease substrate. *Clin Cancer Res.* 2012; 18: 238-47.
- 576 10. Kondo N, Temma T, Deguchi J, Sano K, Ono M, Saji H. Development of PEGylated
577 peptide probes conjugated with 18 F-labeled BODIPY for PET/optical imaging of MT1-MMP
578 activity. *J Control Release.* 2015; 220: 476-83.
- 579 11. van Duijnhoven SM, Robillard MS, Hermann S, Kuhlmann MT, Schäfers M, Nicolay
580 K, et al. Imaging of MMP activity in postischemic cardiac remodeling using radiolabeled
581 MMP-2/9 activatable peptide probes. *Mol Pharm.* 2014; 11: 1415-23.
- 582 12. Gallo J, Kamaly N, Lavdas I, Stevens E, Nguyen QD, Wylezinska-Arridge M, et al.
583 CXCR4-Targeted and MMP-Responsive Iron Oxide Nanoparticles for Enhanced Magnetic
584 Resonance Imaging. *Angewandte Chemie International Edition.* 2014; 53: 9550-4.
- 585 13. Ansari C, Tikhomirov GA, Hong SH, Falconer RA, Loadman PM, Gill JH, et al.
586 Development of Novel Tumor-Targeted Theranostic Nanoparticles Activated by Membrane-
587 Type Matrix Metalloproteinases for Combined Cancer Magnetic Resonance Imaging and
588 Therapy. *Small.* 2014; 10: 566-75.
- 589 14. Yuan Y, Ge S, Sun H, Dong X, Zhao H, An L, et al. Intracellular self-assembly and
590 disassembly of 19F nanoparticles confer respective “Off” and “On” 19F NMR/MRI signals for
591 Legumain activity detection in zebrafish. *ACS Nano.* 2015; 9: 5117-24.
- 592 15. Wang LV, Hu S. Photoacoustic tomography: *in vivo* imaging from organelles to organs.
593 *Science.* 2012; 335: 1458-62.
- 594 16. Taruttis A, Ntziachristos V. Advances in real-time multispectral optoacoustic imaging
595 and its applications. *Nat Photonics.* 2015; 9: 219-27.
- 596 17. Nie L, Chen X. Structural and functional photoacoustic molecular tomography aided by
597 emerging contrast agents. *Chem Soc Rev.* 2014; 43: 7132-70.

- 598 18. Kim C, Favazza C, Wang LV. *In vivo* photoacoustic tomography of chemicals: high-
599 resolution functional and molecular optical imaging at new depths. *Chem Rev.* 2010; 110:
600 2756-82.
- 601 19. Barrett AJ, Woessner JF, Rawlings ND. *Handbook of proteolytic enzymes*: Elsevier;
602 2012.
- 603 20. Levi J, Kothapalli SR, Ma T-J, Hartman K, Khuri-Yakub BT, Gambhir SS. Design,
604 synthesis, and imaging of an activatable photoacoustic probe. *J Am Chem Soc.* 2010; 132:
605 11264-9.
- 606 21. Levi J, Kothapalli S-R, Bohndiek S, Yoon J-K, Dragulescu-Andrasi A, Nielsen C, et al.
607 Molecular photoacoustic imaging of follicular thyroid carcinoma. *Clin Cancer Res.* 2013; 19:
608 1494-502.
- 609 22. Dragulescu-Andrasi A, Kothapalli S-R, Tikhomirov GA, Rao J, Gambhir SS.
610 Activatable oligomerizable imaging agents for photoacoustic imaging of furin-like activity in
611 living subjects. *J Am Chem Soc.* 2013; 135: 11015-22.
- 612 23. Yang K, Zhu L, Nie L, Sun X, Cheng L, Wu C, et al. Visualization of protease activity
613 *in vivo* using an activatable photo-acoustic imaging probe based on CuS nanoparticles.
614 *Theranostics.* 2014; 4: 134.
- 615 24. Zhang L, Gao S, Zhang F, Yang K, Ma Q, Zhu L. Activatable hyaluronic acid
616 nanoparticle as a theranostic agent for optical/photoacoustic image-guided photothermal
617 therapy. *ACS Nano.* 2014; 8: 12250-8.
- 618 25. Miao Q, Pu K. Emerging Designs of activatable photoacoustic probes for molecular
619 imaging. *Bioconjug Chem.* 2016; 27: 2808-23.
- 620 26. Zhang Q, Li W, Moran C, Zeng J, Chen J, Wen L-P, et al. Seed-mediated synthesis of
621 Ag nanocubes with controllable edge lengths in the range of 30– 200 nm and comparison of
622 their optical properties. *J Am Chem Soc.* 2010; 132: 11372-8.

- 623 27. Zhou F, Wu S, Yuan Y, Chen WR, Xing D. Mitochondria-Targeting Photoacoustic
624 Therapy Using Single-Walled Carbon Nanotubes. *Small*. 2012; 8: 1543-50.
- 625 28. Lalwani G, Cai X, Nie L, Wang LV, Sitharaman B. Graphene-based contrast agents for
626 photoacoustic and thermoacoustic tomography. *Photoacoustics*. 2013; 1: 62-7.
- 627 29. Pu K, Shuhendler AJ, Jokerst JV, Mei J, Gambhir SS, Bao Z, et al. Semiconducting
628 polymer nanoparticles as photoacoustic molecular imaging probes in living mice. *Nat*
629 *Nanotechnol*. 2014; 9: 233-9.
- 630 30. Jokerst JV, Thangaraj M, Kempen PJ, Sinclair R, Gambhir SS. Photoacoustic Imaging
631 of Mesenchymal Stem Cells in Living Mice via Silica-Coated Gold Nanorods. *ACS Nano*.
632 2012; 6: 5920-30.
- 633 31. Song L, Zhao N, Xu F-J. Hydroxyl-Rich Polycation Brushed Multifunctional Rare-
634 Earth-Gold Core-Shell Nanorods for Versatile Therapy Platforms. *Adv Funct Mater*. 2017; 27:
635 1701255-n/a.
- 636 32. Zhao N, Li J, Zhou Y, Hu Y, Wang R, Ji Z, et al. Hierarchical Nanohybrids of Gold
637 Nanorods and PGMA-Based Polycations for Multifunctional Theranostics. *Adv Funct Mater*.
638 2016; 26: 5848-61.
- 639 33. Li W, Brown PK, Wang LV, Xia Y. Gold nanocages as contrast agents for photoacoustic
640 imaging. *Contrast Media Mol Imaging*. 2011; 6: 370-7.
- 641 34. Yang X, Skrabalak SE, Li Z-Y, Xia Y, Wang LV. Photoacoustic tomography of a rat
642 cerebral cortex *in vivo* with au nanocages as an optical contrast agent. *Nano Lett*. 2007; 7: 3798-
643 802.
- 644 35. Song KH, Kim C, Cobley CM, Xia Y, Wang LV. Near-infrared gold nanocages as a
645 new class of tracers for photoacoustic sentinel lymph node mapping on a rat model. *Nano Lett*.
646 2008; 9: 183-8.

- 647 36. Kim C, Cho EC, Chen J, Song KH, Au L, Favazza C, et al. *In vivo* molecular
648 photoacoustic tomography of melanomas targeted by bioconjugated gold nanocages. *ACS*
649 *Nano*. 2010; 4: 4559-64.
- 650 37. Xia X, Yang M, Oetjen LK, Zhang Y, Li Q, Chen J, et al. An enzyme-sensitive probe
651 for photoacoustic imaging and fluorescence detection of protease activity. *Nanoscale*. 2011; 3:
652 950-3.
- 653 38. Roy R, Yang J, Moses MA. Matrix metalloproteinases as novel biomarker s and
654 potential therapeutic targets in human cancer. *J Clin Oncol*. 2009; 27: 5287-97.
- 655 39. Yu M, Zheng J. Clearance pathways and tumor targeting of imaging nanoparticles. *ACS*
656 *Nano*. 2015; 9: 6655-74.
- 657 40. Herzog E, Taruttis A, Beziere N, Lutich AA, Razansky D, Ntziachristos V. Optical
658 imaging of cancer heterogeneity with multispectral optoacoustic tomography. *Radiology*. 2012;
659 263: 461-8.
- 660 41. Galanzha EI, Shashkov EV, Spring PM, Suen JY, Zharov VP. *In vivo*, noninvasive,
661 label-free detection and eradication of circulating metastatic melanoma cells using two-color
662 photoacoustic flow cytometry with a diode laser. *Cancer Res*. 2009; 69: 7926-34.
- 663 42. Kim C, Song KH, Gao F, Wang LV. Sentinel lymph nodes and lymphatic vessels:
664 noninvasive dual-modality *in vivo* mapping by using indocyanine green in rats—volumetric
665 spectroscopic photoacoustic imaging and planar fluorescence imaging 1. *Radiology*. 2010; 255:
666 442-50.
- 667 43. Skrabalak SE, Au L, Li X, Xia Y. Facile synthesis of Ag nanocubes and Au nanocages.
668 *Nat Protoc*. 2007; 2: 2182.
- 669 44. Cho EC, Kim C, Zhou F, Cobley CM, Song KH, Chen J, et al. Measuring the optical
670 absorption cross sections of Au–Ag nanocages and au nanorods by photoacoustic imaging. *J*
671 *Phys Chem C*. 2009; 113: 9023-8.

- 672 45. Taraboletti G, D'Ascenzo S, Borsotti P, Giavazzi R, Pavan A, Dolo V. Shedding of the
673 matrix metalloproteinases MMP-2, MMP-9, and MT1-MMP as membrane vesicle-associated
674 components by endothelial cells. *Am J Pathol.* 2002; 160: 673-80.
- 675 46. Chau Y, Padera RF, Dang NM, Langer R. Antitumor efficacy of a novel polymer–
676 peptide–drug conjugate in human tumor xenograft models. *Int J Cancer.* 2006; 118: 1519-26.
- 677